https://doi.org/10.5194/angeo-2020-59
Preprint. Discussion started: 18 August 2020
© Author(s) 2020. CC BY 4.0 License.

Annales Geophysicae Discussions

Ion acoustic waves near a comet nucleus: Rosetta observations at comet 67P/Churyumov-Gerasimenko

Herbert Gunell[1], Charlotte Goetz[2], Elias Odelstad[3], Arnaud Beth[1], Maria Hamrin[1], Pierre Henri[4,5], Fredrik L. Johansson[6], Hans Nilsson[7], and Gabriella Stenberg Wieser[7]

[1]Department of Physics, Umeå University, 901 87 Umeå, Sweden
[2]Space Research and Technology Centre, European Space Agency, Keplerlaan 1, 2201AZ Noordwijk, The Netherlands
[3]Department of Space and Plasma Physics, Royal Institute of Technology, 100 44 Stockholm, Sweden
[4]LPC2E, CNRS, F-45071 Orléans, France
[5]Lagrange, OCA, CNRS, UCA, Nice, France
[6]Swedish Institute of Space Physics, Box 537, 751 21 Uppsala, Sweden
[7]Swedish Institute of Space Physics, Box 812, 981 28 Kiruna, Sweden

Correspondence: Herbert Gunell (herbert.gunell@physics.org)

Abstract. Ion acoustic waves were observed between 15 and 30 km from the centre of comet 67P/Churyumov-Gerasimenko by the Rosetta spacecraft during its close flyby on 28 March 2015. There are two electron populations: one cold at $k_\mathrm{B}T_\mathrm{e} \approx 0.2\,\mathrm{eV}$ and one warm at $k_\mathrm{B}T_\mathrm{e} \approx 4\,\mathrm{eV}$. The ions are dominated by a cold (a few hundredths of eV) distribution with a bulk speed of $(3–3.7)\,\mathrm{km\,s^{-1}}$. Near closest approach the propagation direction was within $50°$ from the direction of the bulk velocity, leading to a Doppler shift of the waves that in the spacecraft frame cover a frequency range up to approximately 4 kHz. The wave power decreased over cometocentric distances from 24 to 30 km. The main difference between the plasma at closest approach and in the region where the waves are decaying is the absence of a significant current in the latter.

1 Introduction

Observations of waves can give us information of the plasma in which they are generated and through which they have travelled. Waves are also of general interest in plasma physics as they provide a means for energy transfer and because they affect the particle distributions through wave–particle interaction processes. When comets 21P/Giacobini-Zinner and 1P/Halley were visited by spacecraft in the 1980s a variety of plasma waves were reported (Scarf et al., 1986c, a; Scarf, 1989). Among these observations were ion acoustic waves, detected both in the bow shock region (Scarf et al., 1986b) and upstream (Oya et al., 1986).

The Rosetta spacecraft (Glassmeier et al., 2007a) accompanied comet 67P/Churyumov-Gerasimenko for two years from August 2014 to September 2016. Shortly after the spacecraft reached the comet, low frequency ($f \lesssim 100\,\mathrm{mHz}$) long wavelength ($100\,\mathrm{km} \lesssim \lambda \lesssim 700\,\mathrm{km}$) waves were detected in the magnetic field data (Richter et al., 2015, 2016). These were named “singing

https://doi.org/10.5194/angeo-2020-59
Preprint. Discussion started: 18 August 2020
© Author(s) 2020. CC BY 4.0 License.

comet" waves; they have been interpreted in terms of a modified ion-Weibel instability (Meier et al., 2016), found to be compressional (Breuillard et al., 2019), and detected as far as 800 km from the nucleus (Goetz et al., 2020). Waves in the lower hybrid frequency range ($f \lesssim 15\,\mathrm{Hz}$) were found by André et al. (2017) and Karlsson et al. (2017). Lower hybrid waves were frequently seen in bursts in connection with density gradients, oscillating on minute time scales (Stenberg Wieser et al., 2017). These minute time scale oscillations are known as steepened waves, and they were observed outside the diamagnetic cavity (Goetz et al., 2016b, a). Electric field measurements showed waves in the lower hybrid frequency range on both sides of the diamagnetic cavity boundary, indicating a mode conversion between lower hybrid waves and ion acoustic waves (Madsen et al., 2018).

Ion acoustic waves are compressional plasma waves that are weakly damped only when $T_\mathrm{e} \gg T_\mathrm{i}$ and the frequency is below the ion plasma frequency. In this limit, ω is proportional to k and the phase speed is $c_\mathrm{s} = \sqrt{k_\mathrm{B} T_\mathrm{e}/m_\mathrm{i}}$ (see for example Krall and Trivelpiece, 1973). As the frequency approaches the ion plasma frequency they become increasingly heavily damped and also the phase speed decreases. If the ion and electron temperatures are similar, this also leads to heavy damping, and ion acoustic waves are usually not detectable in that regime. Ion acoustic waves were observed by the Rosetta spacecraft on 20 January 2015 (Gunell et al., 2017b) at approximately 2.5 AU from the Sun, before the diamagnetic cavity had formed, and also in the diamagnetic cavity near perihelion (Gunell et al., 2017a). The ion acoustic waves seen in the cavity were interpreted as a result of part of the current at the diamagnetic cavity boundary closing through bulges on that boundary and generating waves through a current–driven instability (Gunell et al., 2017a).

In this article, we examine ion acoustic waves detected by Rosetta during its close flyby of comet 67P on 28 March 2015. The comet was at a heliocentric distance of 2.0 AU at the time, and the gas production rate varied between $3 \times 10^{26}\,\mathrm{s}^{-1}$ and $9 \times 10^{26}\,\mathrm{s}^{-1}$ during the day. Magnetic pileup and draping has been studied before for this flyby, both in observational studies and using hybrid simulations (Koenders et al., 2016). The magnetic field piled up near the nucleus, causing the solar wind protons to be deflected out of the ecliptic plane. This in turn caused the draped magnetic field in the region near the nucleus to align itself with the deflected solar wind flow. No sign of a diamagnetic cavity was seen during the flyby, and that was likely due to it not having formed yet. The hybrid simulations of the flyby presented by Koenders et al. (2016) show the presence of an infant bow shock (Gunell et al., 2018) approximately 100 km from the nucleus, but that is farther out than the spacecraft reached on that day.

2 Observations

We use the comet-centred solar equatorial coordinate system (CSEQ) throughout this article. In this system, the x axis points from the comet to the Sun, the z axis is the component of the rotation axis of the Sun that is perpendicular to the x axis, and the y axis is directed to complete the right-handed coordinate system. The spacecraft moved from negative to positive y and z values at a nearly constant $x = 11\,\mathrm{km}$. The spacecraft trajectory is illustrated in Fig. 1.

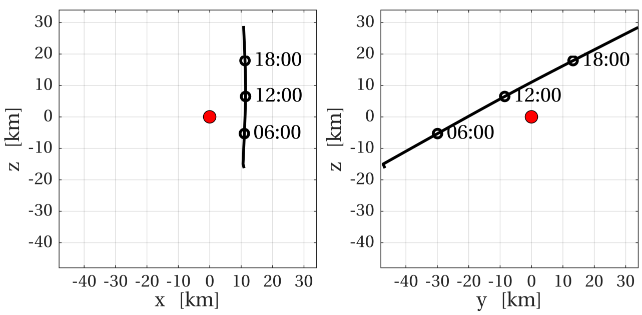

Figure 1. Trajectory followed by the Rosetta spacecraft during the close flyby on 28 March 2015. The red circle represents the nucleus of comet 67P/Churyumov-Gerasimenko.

The closest approach occured at 13:05 UTC, and then Rosetta was at a cometocentric distance of 15 km. The spacecraft moved slowly (with a relative speed to the comet below $1\,\mathrm{ms}^{-1}$) and was in the the vicinity of the nucleus for several hours as shown in Fig. 1 and in panel h of Fig. 2.

2.1 Instrumentation

The data used in this article was obtained by instruments belonging to the Rosetta Plasma Consortium (RPC) (Carr et al., 2007). For the wave observations (Sect. 2.2) we used the Rosetta Langmuir probe instrument (RPC-LAP) (Eriksson et al., 2007) to record time series of plasma waves in the cometary plasma environment. Starting at 10:55:34 on 28 March 2015, RPC-LAP regularly recorded such time series for the rest of the day. The probe current was sampled at a frequency of $f_\mathrm{s} = 18750\,\mathrm{Hz}$, and each time series contains 1600 samples, corresponding to a time series length of 85.3 ms. This process was repeated every 160 s. Each of the two probes obtained 295 such time series during the day. The power spectral density for each time series is computed, using Welch's method (Welch, 1967), averaging segments that are 256 samples long with an overlap of 65 % (Fig. 2a and b). The probes were held at fixed potentials with respect to the spacecraft: probe 1 at $+30\,\mathrm{V}$ and probe 2 at $-30\,\mathrm{V}$. The Langmuir probe instrument was also used to measure the bulk speed of the ions and the electron temperature by sweeping the probe potential and measuring the probe current as described in Sect. 2.3.

We use the Mutual Impedance Probe (RPC-MIP) (Trotignon et al., 2007) to obtain the plasma density during the flyby. The RPC-MIP instrument observes the plasma frequency, from which the plasma density is derived (Fig. 2f). The ion populations are sampled by the Ion Composition Analyser (RPC-ICA) (Nilsson et al., 2007) (Fig. 2g). The magnetic field is measured by the magnetometer (RPC-MAG) (Glassmeier et al., 2007b). The components are presented in CSEQ coordinates in Fig. 2d. How the properties of the plasma are derived from the data collected by these instruments is described in Sect. 2.3.

https://doi.org/10.5194/angeo-2020-59
Preprint. Discussion started: 18 August 2020
© Author(s) 2020. CC BY 4.0 License.
Annales Geophysicae Discussions

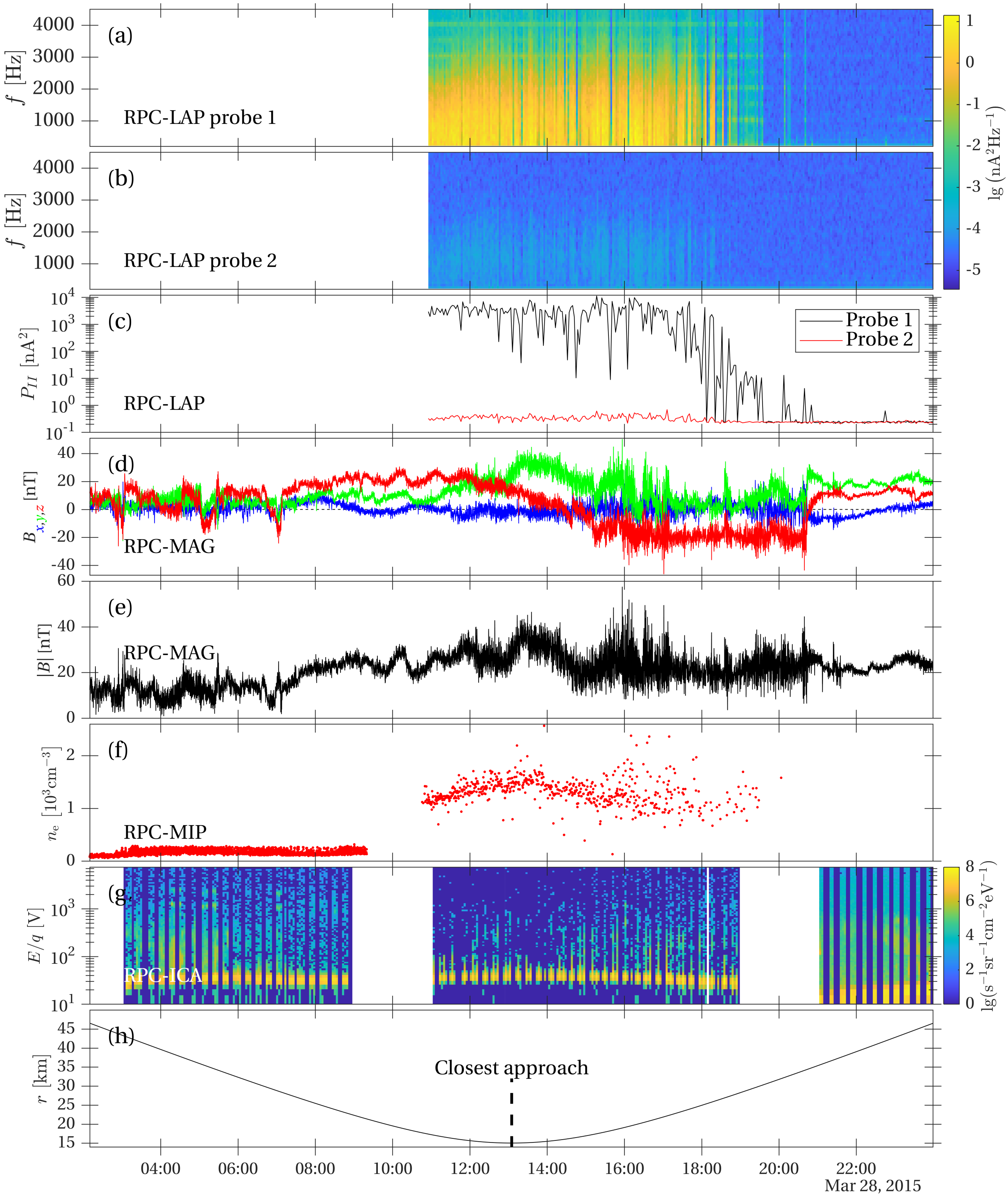

Figure 2. Rosetta observations during the close flyby of comet 67P/Churyumov-Gerasimenko on 28 March 2015. (a) Power spectral density of RPC-LAP probe 1 in the frequency range 200 Hz $< f <$ 4.5 kHz. (b) Power spectral density of RPC-LAP probe 2 in the same frequency range. (c) The power spectral density of probes 1 and 2 integrated from 200 Hz to the Nyquist frequency of 9375 Hz. (d) B_x (blue), B_y (green), and B_z (red) components of the magnetic flux density measured by RPC-MAG. (e) The magnitude of the magnetic flux density. (f) The plasma density measured by RPC-MIP. (g) Ion energy spectrum observed by RPC-ICA summed over all angles and mass channels. (h) Cometocentric distance of the Rosetta spacecraft.

https://doi.org/10.5194/angeo-2020-59
Preprint. Discussion started: 18 August 2020
© Author(s) 2020. CC BY 4.0 License.

2.2 Waves

Power spectral densities obtained for RPC-LAP probe 1 are shown in Fig. 2a, and those recorded by probe 2 are shown in Fig. 2b. The colour coded quantity is the logarithm of the power spectral density (PSD) of the probe currents. The lowest frequency bins are at risk of picking up low-frequency noise, and we therefore show the spectrum for frequencies above 200 Hz. There may be other waves present at low frequencies, but in this article we only consider ion acoustic waves above 200 Hz.

A high amplitude wave signal is seen during the close flyby and it falls off as the spacecraft moves away from the nucleus. The power spectral density of the positively biased probe 1 is several orders of magnitude higher than that of the negative probe 2. This means that the probe 1 signal is dominated by the electron current and that the signal is proportional to the density variation of the wave. The probe was thus operating in the same regime as when waves were observed in the diamagnetic cavity when the comet was at perihelion (Gunell et al., 2017a). Also the maximum PSD value is similar to those observations and the plasma density, shown here in Fig. 2f, was in both cases somewhat above $1000\,\mathrm{cm}^{-3}$. The situation differs from the first ion acoustic wave observations at comet 67P (Gunell et al., 2017b) when the plasma density was an order of magnitude smaller and the waves coupled capacitively to the probe through the displacement current instead of a particle current. The difference between the probes is also seen in Fig. 2c, which shows the integral of the power spectral density over frequencies from 200 Hz up to the Nyquist frequency.

Fig. 3 shows four sample spectra of the probe 1 current for frequencies from 200 Hz up to the Nyquist frequency. There is wave power starting at the low end of this frequency range with a broad maximum in the vicinity of $1\,\mathrm{kHz}$, and at higher frequencies the PSD declines toward the noise floor. The black curve shows the PSD at 13:24:54, which is near closest approach to the comet nucleus at a cometocentric distance of $15\,\mathrm{km}$. As seen in Fig. 2c the total wave power fluctuated but remained at a generally high level while the spacecraft was in the near-nucleus environment. The PSD obtained at 15:16:54 (red curve in Fig. 3) is another example from this period. The spacecraft was at $17.5\,\mathrm{km}$ cometocentric distance and the wave power was even higher than that shown by the black curve. The wave power declined as the spacecraft moved to larger cometocentric distances. This process started approximately at 17:45 when Rosetta was at 24 km from the centre of the nucleus. Two examples from the declining phase are shown in Fig. 3: the spectrum obtained at 17:56:54 at 25 km (blue curve) and one spectrum from 19:08:54 at 29 km (green curve) when the wave power had fallen even more. The two curves that will be used for comparison with wave theory in Sect. 3 are the black curve (13:24:54) for closest approach and the blue curve (17:56:54) for the outbound case. The peaks at multiples of 1 kHz seen in the frequency range where the wave power is low, both in Fig. 3) and Fig. 2 are artefacts generated by the spacecraft.

2.3 Plasma properties

To analyse the waves we need to know the basic properties of the plasma. The plasma density obtained by the mutual impedance probe, RPC-MIP, is shown in Fig. 2f. The density peaks around closest approach and then falls off as the spacecraft moves away from the nucleus. The scattered instantaneous plasma density values are a signature of strong plasma inhomogeneities of

https://doi.org/10.5194/angeo-2020-59
Preprint. Discussion started: 18 August 2020
© Author(s) 2020. CC BY 4.0 License.

Annales Geophysicae
Discussions

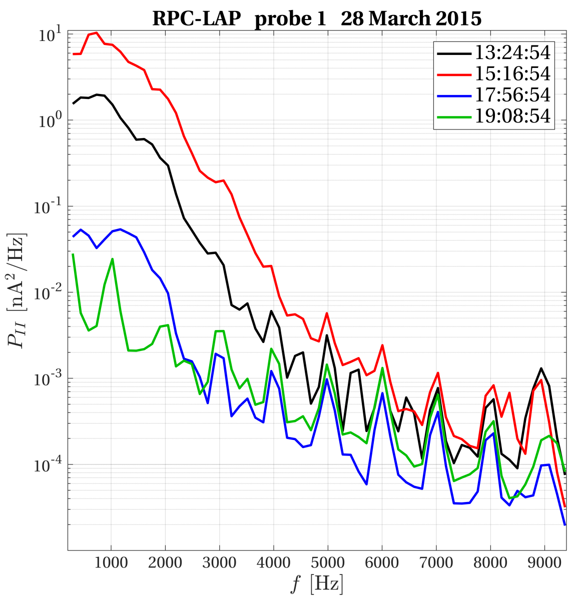

Figure 3. Power spectral densities from 200 Hz up to the Nyquist frequency for the RPC-LAP probe 1 current for four different times during the Rosetta close flyby of comet 67P. The black curve (13:24:54) is used in Sect. 3 for analysis of waves near closest approach and the blue curve (17:56:54) for similar analysis of during the outbound part of the flyby.

approximately 10 % around closest approach. For the calculations in Sect. 3 we estimate a plasma density of $n_\mathrm{e} = 1600\,\mathrm{cm}^{-3}$ at closest approach and $n_\mathrm{e} = 1000\,\mathrm{cm}^{-3}$ for the outbound case.

Fig. 2g shows an energy spectrum of the ions observed by RPC-ICA. Starting at $E/q \approx 20\,\mathrm{V}$ is a warm ($k_\mathrm{B}T_\mathrm{i} \approx 6\,\mathrm{eV}$ around the time of closest approach) water ion population, which has been accelerated toward the spacecraft due to the negative spacecraft potential. Some accelerated water ions are seen at higher energies, but the vast majority of the ions seen in Fig. 2g belong to the warm, low energy, population. Fitting the observed flux to a Maxwellian distribution we arrive at a density estimate of about $4\,\mathrm{cm}^{-3}$ for this ion population. However, this is far below the $1600\,\mathrm{cm}^{-3}$ plasma density measured by RPC-MIP. It was shown by Bergman et al. (2020a, b) that low energy (down to 5 eV) ions describe complicated orbits in the potential well around the spacecraft. Therefore the field of view of the instrument may be far from what is nominally expected, and the low energy part of the observed distribution functions can be very inaccurate. The field of view for ions with lower energies than the $5\,\mathrm{eV}$ lower limit considered by Bergman et al. (2020a, b) is even more limited, and the fraction of that population that is detected may not be distinguishable from ions belonging to the warm population. Thus, the discrepancy between the RPC-ICA measured ion density and the plasma density measured by RPC-MIP may be explained by a cold water ion distribution that is invisible to RPC-ICA.

This is confirmed by Langmuir probe characteristics shown in Fig. 4. The left panel shows the part of the characteristics dominated by the ion current. For a cold ion population drifting at a bulk speed u the probe current I depends on the probe to

https://doi.org/10.5194/angeo-2020-59
Preprint. Discussion started: 18 August 2020
© Author(s) 2020. CC BY 4.0 License.
Annales Geophysicae Discussions
Open Access
EGU

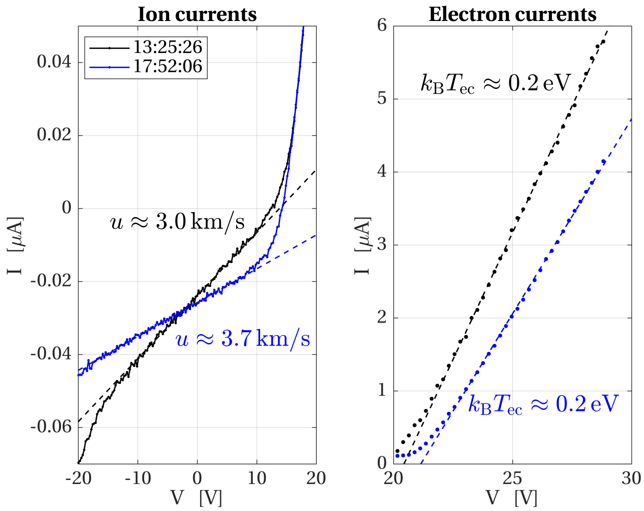

Figure 4. I–V traces from RPC-LAP near closest approach (black) and during the outbound part of the flyby (blue). The left-hand panel shows the ion currents and the right-hand panel the electron currents. The dashed lines have been fitted to the I–V traces to estimate the bulk speed of the cold ion population and the temperature of the cold electron population.

plasma potential V according to (Mott-Smith and Langmuir, 1926)

$$I = -\pi r_\mathrm{p}^2 n_\mathrm{i} u e \left(1 - \frac{2eV}{m_\mathrm{i} u^2}\right), \tag{1}$$

where $r_\mathrm{p} = 2.5\,\mathrm{cm}$ is the radius of the probe, m_i is the ion mass and n_i the ion density. We fit a line to the linear part of the curve, and taking the derivative of Eq. (1) and rearranging we can determine the drift velocity from the slope $\mathrm{d}I/\mathrm{d}V$ of that line:

$$u = \frac{2 n_\mathrm{i} e^2 \pi r_\mathrm{p}^2}{m_\mathrm{i} \frac{\mathrm{d}I}{\mathrm{d}V}}. \tag{2}$$

Taking the ion density to be equal to the plasma density measured by RPC-MIP we arrive at an ion drift speed of $3\,\mathrm{km\,s^{-1}}$ near closest approach and $3.7\,\mathrm{km\,s^{-1}}$ at 17:52:06 when the spacecraft was moving outward as shown in Fig. 4. These numbers are within the range of those observed by Odelstad et al. (2018). The velocity obtained from Eq. (2) is a upper limit, as it is based on the assumption of cold, zero temperature, ions. The ion temperature can be estimated from the neutral temperature, as ions are created by ionisation of the neutrals. Biver et al. (2019) found neutral temperatures in the 50–200 K range, which corresponds to approximately $0.02\,\mathrm{eV}$, and that is well below the $1\,\mathrm{eV}$ kinetic energy, corresponding to the 3–3.7 $\mathrm{km\,s^{-1}}$ drift speeds obtained above.

The right-hand panel of Fig. 4 shows the part of the probe characteristic where the current is dominated by the electrons. The dashed lines have been fitted to the high probe potential part of the sweep. Here, the current varies linearly with voltage

https://doi.org/10.5194/angeo-2020-59
Preprint. Discussion started: 18 August 2020
© Author(s) 2020. CC BY 4.0 License.
Annales Geophysicae Discussions

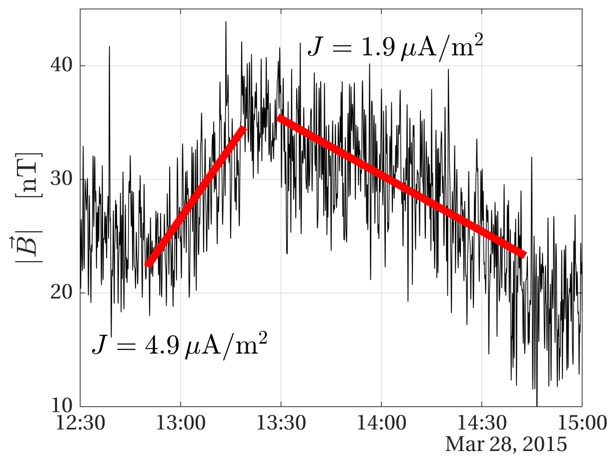

Figure 5. Magnetic field magnitude during a period around closest approach. The red lines are fitted to the data in order to derive the current densities $J = 4.9\,\mu\text{A m}^{-2}$ (inbound) and $J = 1.9\,\mu\text{A m}^{-2}$ (outbound).

(Swift and Schwar, 1970) and the cold electron temperature is (Engelhardt et al., 2018)

$$T_\mathrm{e} = 8\pi \frac{r_\mathrm{p}^4 e^3 n_\mathrm{e}^2}{m_\mathrm{e}} \left(\frac{\mathrm{d}I}{\mathrm{d}V}\right)^{-2}. \tag{3}$$

The slopes of these lines correspond to temperatures of $k_\mathrm{B}T_\mathrm{e} = 0.2\,\mathrm{eV}$ for both the closest approach and outbound curves. The curves also show that the plasma potential is between 12 and 14 volts above the spacecraft potential, approximately. For the spacecraft to become that negatively charged there must be an additional electron population which is warmer. The estimate we use in Sect. 3 is that the electron distribution is constituted by two contributions with equal densities: one cold with temperatures as estimated in Fig. 4 and one warm with a temperature of 4 eV. This follows previous Langmuir probe sweep interpretations from when the comet was near perihelion (Eriksson et al., 2017; Gunell et al., 2017a; Odelstad et al., 2018) with the difference that the cold electrons are not quite as cold here as the 0.1 eV that was estimated near perihelion. These two electron temperature values are within the range of those observed by RPC-MIP at similar heliocentric distances in 2016 (Wattieaux et al., 2020).

Figure 2d shows the components and Fig. 2e the magnitude of $\mathbf{B}$ as measured by RPC-MAG. The magnitude of the magnetic field increased as the spacecraft approached the centre of the comet and decreased as it was moving away. This is expected from magnetic pileup and field line draping, but there are also other changes in the magnetic field that can be seen in Fig. 2d and e.

To estimate the current associated with the non-uniformity of the magnetic field we fit lines to the magnitude of the magnetic field as shown in Fig. 5. Then we estimate the magnitude of the current density by

$$J = \frac{|\Delta B|}{\mu_0 |\Delta \mathbf{r}|}.$$

https://doi.org/10.5194/angeo-2020-59
Preprint. Discussion started: 18 August 2020
© Author(s) 2020. CC BY 4.0 License.

where $|\Delta B|$ is the change in the fitted magnetic field magnitude and $|\Delta \mathbf{r}|$ is the distance the spacecraft moved during the same period of time. This yields a current density of $J = 4.9\,\mu\mathrm{A\,m^{-2}}$ when the spacecraft was approaching the nucleus and $J = 1.9\,\mu\mathrm{A\,m^{-2}}$ while it was moving away. These values should be seen as estimates of the average current density. Koenders et al. (2016) compared the magnetic field observed during this flyby to the magnetic field obtained in hybrid simulations and found good agreement for B_y, which is the dominating component. The simulated B_z component was about a factor of 2 lower than what was observed by Rosetta. The difference could be attributed to the limited resolution or the use of an averaged outgassing profile in the simulations (Koenders et al., 2016). For the magnitude of $\mathbf{B}$ the difference only amounts to 10–20 %, but the simulation does not follow how the plasma quantities develop in time. Fig. 5 shows that the magnetic field changed on much shorter timescales than those of our linear approximations during the flyby. From a single spacecraft measurement we cannot determine whether these magnetic field fluctuations are due to local variations of the current in the plasma or whether the whole inner region of the ionised coma is undergoing oscillations. Thus, the current density may have been both higher and lower than these average values during the flyby.

2.4 Typical scales

A plasma density of $1600\,\mathrm{cm^{-3}}$ corresponds to an electron plasma frequency of approximately 350 kHz and a H_2O^+ ion plasma frequency of 2 kHz. Thus, electron time scale waves, such as Langmuir waves and electron acoustic waves, are far beyond reach of our observations, the Langmuir probe being sampled at the much lower frequency of 18.75 kHz. Ion acoustic waves, on the other hand, are in the accessible frequency range. The magnetic field during the flyby varied between 20 and 40 nT approximately. This corresponds to electron cyclotron frequencies between 0.6 and 1.1 kHz, which is in the middle of the observed frequency range. However, the wave frequency does not follow the changes in the magnetic field, which rules out electron cyclotron waves. The ion cyclotron frequency is $(0.02 - 0.03)\,\mathrm{Hz}$, which is below the frequencies we can resolve.

The spacecraft was at 15 km cometocentric distance at closest approach and at 25 km at 18:00 when the wave amplitude started to decrease. Thus, the typical length for the variation in wave amplitude is about 10 km. Assuming a typical B of 30 nT warm ions at 6 eV would have a gyroradius of 50 km. Cold ions are picked up by the electric field, moving along trajectories with a radius of curvature that is even larger. The ions can thus be seen as unmagnetised. Warm electrons at 4 eV have gyroradius of 225 m and for cold 0.2 eV electrons the gyroradius is 50 m approximately.

In Sect. 3 we use kinetic theory to compute dispersion relations for electrostatic waves in an unmagnetised plasma. This is applicable if the wavelength is much shorter than the gyroradii of the particles so that the influence of magnetic forces on particle motion is negligible on wavelength scales. In Sect. 3 it is seen that the phase speed for ion acoustic waves is approximately $1.7\,\mathrm{km\,s^{-1}}$. Thus, a wave at 200 Hz (the lower limit of the spectrum shown in Fig. 2a) has a wavelength of 8.5 m, which is far below all the gyroradii reported above. The assumption that the plasma is unmagnetised for wave purposes holds above that limit, and these are the waves considered here. For waves at the very lowest frequencies, below the range considered here, the wavelength is longer, and electromagnetic effects would have to be taken into account.

https://doi.org/10.5194/angeo-2020-59
Preprint. Discussion started: 18 August 2020
© Author(s) 2020. CC BY 4.0 License.
Annales Geophysicae Discussions Open Access EGU

Table 1. Parameters of the distributions used in the examples related to the plasma at closest approach.

	cold ions			warm ions			cold electrons			warm electrons		
distr.	n	$k_{\mathrm{B}}T$	v_{D}	n	$k_{\mathrm{B}}T$	v_{D}	n	$k_{\mathrm{B}}T$	v_{D}	n	$k_{\mathrm{B}}T$	v_{D}
	$[\mathrm{cm}^{-3}]$	[eV]	$[\mathrm{km\,s}^{-1}]$	$[\mathrm{cm}^{-3}]$	[eV]	$[\mathrm{km\,s}^{-1}]$	$[\mathrm{cm}^{-3}]$	[eV]	$[\mathrm{km\,s}^{-1}]$	$[\mathrm{cm}^{-3}]$	[eV]	$[\mathrm{km\,s}^{-1}]$
	Closest approach											
1	1554	0.02	0	4	6	0	779	0.2	39.3	779	4	0
2	1558	0.02	0	0	–	–	779	0.2	39.3	779	4	0
3	1518	0.02	0	40	6	0	779	0.2	39.3	779	4	0
4	1558	0.02	0	0	–	–	779	0.2	0	779	4	39.3
5	1558	0.02	0	0	–	–	779	0.2	39.3	779	1	0
6	1558	0.01	0	0	–	–	779	0.2	39.3	779	4	0
7	1558	0.04	0	0	–	–	779	0.2	39.3	779	4	0
	Outbound											
A	1006	0.02	0	0	–	–	503	0.2	23.6	503	4	0
B	1006	0.02	0	0	–	–	503	0.2	0	503	4	0

3 Dispersion relations

Because of the uncertainty at which both electron and ion distribution functions are known, we have calculated dispersion relations under several different assumptions about these distributions. We then compare the results of the calculations with the wave observations in order both to arrive at an explanation for how the waves are generated and to put constraints on what we can say about the charged particle distributions. The total distribution function is composed of a cold and a warm electron and a cold and a warm ion distribution. The parameters are shown in Table 1 for 7 test cases used to model the distribution near closest approach and 2 cases for the outbound trajectory. We use the simple pole expansion method to compute the dispersion relations (Löfgren and Gunell, 1997; Gunell and Skiff, 2001, 2002; Tjulin et al., 2000; Tjulin and André, 2002). In a comet context it was reviewed by Gunell et al. (2017b, also providing the computer code for the computations). Each component of the distribution function is modelled by an approximate Maxwellian,

$$M_m(v) = \left[1 + \frac{(v-v_{\mathrm{d}})^2}{2v_{\mathrm{t}}^2} + \ldots + \frac{1}{m!}\left(\frac{(v-v_{\mathrm{d}})^2}{2v_{\mathrm{t}}^2}\right)^m\right]^{-1}, \tag{4}$$

where v_{t} is the thermal speed, v_{d} is the drift speed, and m is the number of terms included in the expansion. The expression inside the brackets of Eq. (4) is the reciprocal of a Taylor expansion of

$$\exp\left((v-v_{\mathrm{d}})^2/\left(2v_{\mathrm{t}}^2\right)\right).$$

https://doi.org/10.5194/angeo-2020-59
Preprint. Discussion started: 18 August 2020
© Author(s) 2020. CC BY 4.0 License.

Annales Geophysicae
Discussions

As m tends to infinity $M_m(v)$ approaches a Maxwellian, and for small values of m the distributions have suprathermal tails. In the distributions in Table 1, $m = 3$ for the ions and $m = 5$ for the electrons. The influence of suprathermal tails is evaluated in Appendix A.

Fig. 6. shows dispersion relations for the 7 test cases that correspond to the observations near closest approach. We are assuming a real wave number k and a complex angular frequency ω. Panel (a) shows the real part of ω, and panel (b) shows the damping rate γ. Negative values of γ correspond to wave growth. Panel (c) shows the shaded rectangle in panel (b) in more detail. Several of the curves are so similar they fall on top of each other and are difficult to distinguish in the figure. In all cases the least damped or fastest growing mode is the ion acoustic mode and that is the one shown.

The density of the warm ion population is varied in distributions 1–3. In distribution 1 the warm ion density is $4\,\mathrm{cm}^{-3}$ as estimated in Sect. 2.3. In distribution 2 the warm ion density is assumed to be zero, and in distribution 3 the warm ion density is ten times higher than the estimate in Sect. 2.3. The real part of the dispersion relation is indistinguishable among the three cases, as seen in Fig. 6a. The damping rates in Fig. 6c are very close in the three cases, although it can be descried that distribution 3, with the highest warm ion density, has a slightly smaller growth rate than the other two. However, the difference is small, and we conclude that the warm ion population only has a negligible influence on the waves. Therefore, the warm ion density is set to zero in the rest of the distribution functions.

We have used the current density estimate, $J = 4.9\,\mu\mathrm{A\,m}^{-2}$, obtained in Sect. 2.3 for the inbound part of the flyby. The dispersion relations are computed in the rest frame of the ions and the current is modelled by assigning a drift velocity, $|\mathbf{v}_\mathrm{D}| = 39.3\,\mathrm{km\,s}^{-1}$, to one of the electron populations. In distribution 2 and distribution 4 that drift speed is given to the cold and warm electron distribution, respectively. For distribution 4 the ion acoustic mode is damped, while it is growing for distribution 2. We conclude that to drive the ion acoustic waves unstable the current must be carried by the cold electrons.

In distribution 5, the temperature of the warm electrons has been decreased to $1\,\mathrm{eV}$. This leads to a decreased growth rate compared to distribution 2, which has $4\,\mathrm{eV}$ warm electrons but otherwise is equal to distribution 5. However, in both cases the waves are unstable over approximately the same wavelength range.

Distributions 6 and 7 have 0.01 eV and 0.04 eV cold ions, respectively, that is to say, in distribution 6 the ions are colder and in distribution 7 warmer than they are in the otherwise equal distribution 2. This affects the growth rate so that distributions with colder ions grow faster and over a wider k range than distributions where the ions are warmer (Fig. 6c). Also the real part of ω is affected, as shown in Fig. 6a, but this is significant only for k values larger than the k which corresponds to maximum growth. The influence of suprathermal particles on the dispersion relations and growth rates is evaluated in Appendix A, and it is found to similar to the difference between distribution with 0.01 and 0.02 eV ions. The distribution function of the cold ions cannot be measured directly, and hence effects caused by the shape of the distribution cannot be distinguished from effects caused by the temperature alone. However, we may conclude from all 7 cases that any process that gives the ions higher or the electrons lower energy will lead to decreased growth or increased damping.

Dispersion relations for distributions A and B, detailed in Table 1, are shown in Fig. 7. These distributions correspond to the plasma parameters obtained during the outbound passage of the spacecraft, and close to when the PSD represented by the blue line in Fig. 3 was recorded at 17:56:54. In distribution A the cold electrons have been given a drift velocity corresponding to the

https://doi.org/10.5194/angeo-2020-59
Preprint. Discussion started: 18 August 2020
© Author(s) 2020. CC BY 4.0 License.
Annales Geophysicae
Discussions

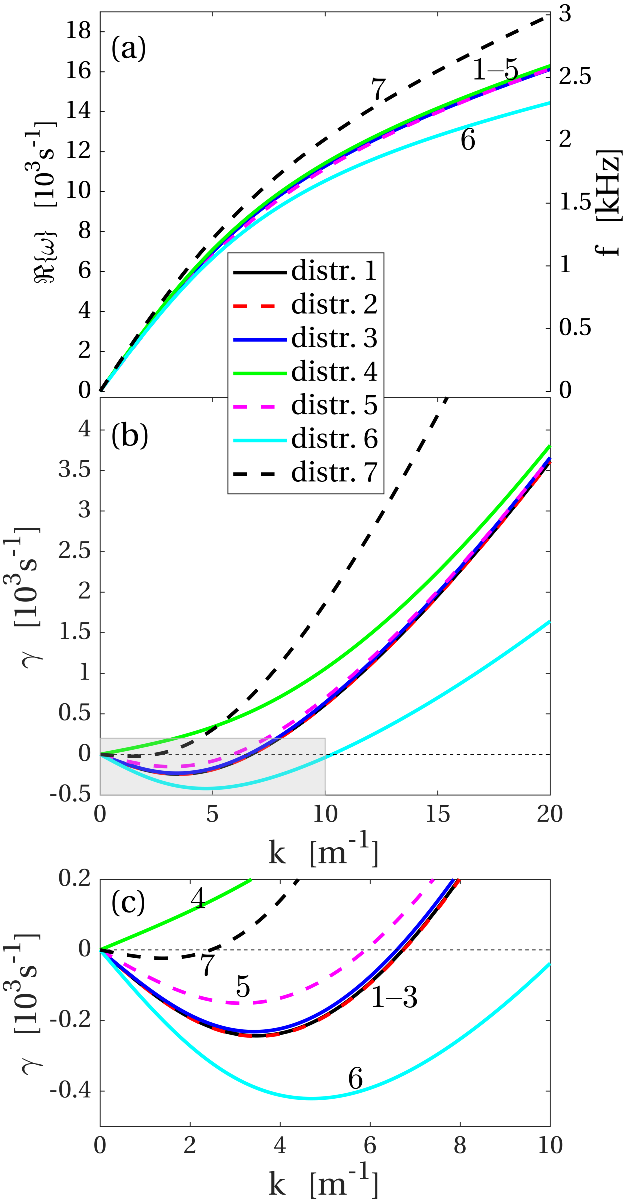

Figure 6. Dispersion relations at closest approach for the seven assumed distributions specified in Table 1. (a) real part of the dispersion relation. (b) damping rate γ. (c) zoom-in on the shaded rectangle in panel (b). The numbers next to the curves identify the different distribution functions shown in Table 1.

https://doi.org/10.5194/angeo-2020-59
Preprint. Discussion started: 18 August 2020
© Author(s) 2020. CC BY 4.0 License.

Annales Geophysicae Discussions

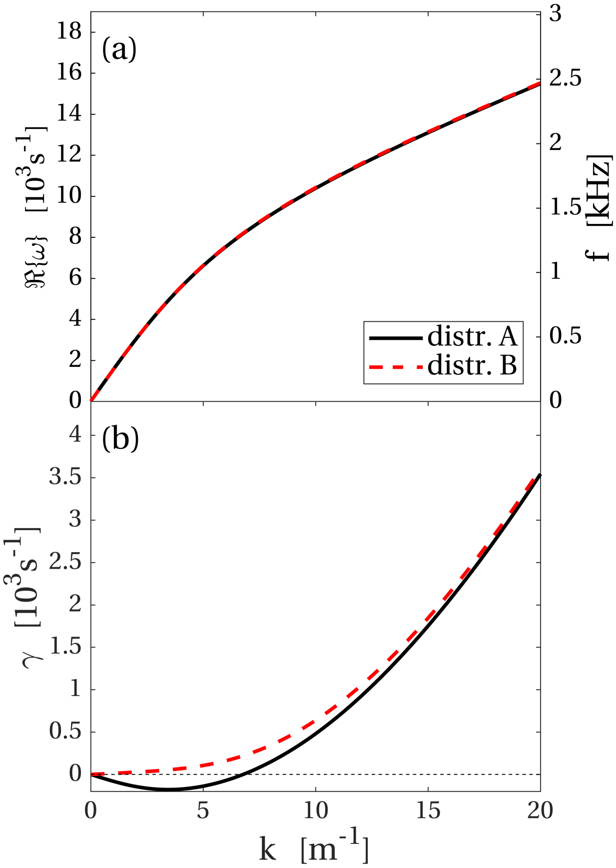

Figure 7. Dispersion relations while the spacecraft was outward bound based on assumed distributions specified in Table 1. (a) real part of the dispersion relation. (b) damping rate γ.

current density $J = 1.9\,\mu\mathrm{A\,m}^{-2}$ measured when the spacecraft was moving away, and the dispersion relation corresponding to distribution A is very similar to those at closest approach. In distribution B none of the populations have been assigned a drift velocity. This leads to a stable distribution, and the waves are weakly damped instead of growing. Examining the magnetic field in Fig. 2 we see no large scale change near 18:00, which means that there was no large scale current present. Thus, the change in the plasma that affects the waves is the absence of a current, and this indicates that the reason why the wave spectrum fades out as the spacecraft moves away from the nucleus is the decline of the current density. Around 18:00 the waves likely were propagating to the spacecraft from a source region closer to the nucleus, where the current density was still high enough to generate the waves.

© Author(s) 2020. CC BY 4.0 License.
Annales Geophysicae Discussions Open Access EGU

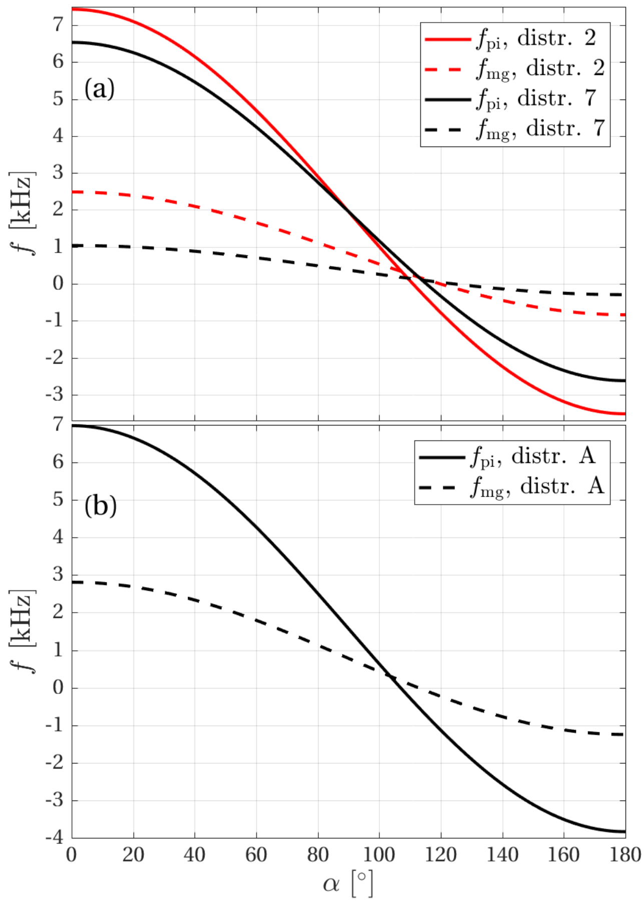

Figure 8. Doppler shifted ion plasma frequencies and frequencies of maximum growth (a) at closest approach and (b) during the outbound motion of the spacecraft. The dispersion relations used to compute the Doppler shift correspond to distributions 2, 7, and A in Table 1.

4 Doppler shift

The dispersion relations are computed in the ion frame of reference and the observations are, by necessity, performed in a spacecraft-fixed frame. A frequency f_{m} in the moving medium is Doppler shifted to frequency f_{sc} in the spacecraft frame according to

$$f_{\mathrm{sc}} = \frac{v_{\mathrm{ph}}(f_{\mathrm{m}}) + u\cos(\alpha)}{v_{\mathrm{ph}}(f_{\mathrm{m}})} f_{\mathrm{m}}, \tag{5}$$

where v_{ph} is the phase velocity given by the dispersion relation, u is the speed of the moving medium, and α is the angle between the wave direction of propagation and the velocity $\mathbf{u}$. Fig. 8a shows the H_2O^+ ion plasma frequency and the frequency of maximum growth, Doppler shifted to the spacecraft frame according to Eq. (5) for the dispersion relations that correspond to distributions 2 and 7, and with u determined by Eq. (2). The frequencies are shown as functions of the angle α. The angle is not known from observations, but by comparing the Doppler shifted frequencies to the observed spectrum we can assess what values of α would lead to a reasonable spectrum.

The dispersion relations show that the damping is considerable at the ion plasma frequency. This has also been seen in experiments with current-driven ion acoustic waves, where the power declines with frequency and reaches the noise floor at frequencies well below the ion plasma frequency (Kawai et al., 1978). For our near closest approach sample spectrum shown by the black curve in Fig. 3 this happens at approximately 5 kHz. The range of angles α consistent with the observed spectra can then be constrained to those for which the ion plasma frequency is mapped to frequencies above 5 kHz. If the waves follow the dispersion relation corresponding to distribution 2, (solid red curve in Fig. 8a) this means that $\alpha \lesssim 56°$ and in the case of distribution 7 (solid black curve in Fig. 8a) the angle is restricted to $\alpha \lesssim 48°$. We will round this off to $\alpha \lesssim 50°$.

For a particular dispersion relation to be in agreement with observations, there should be significant wave power at the Doppler shifted frequency of maximum growth. With this regard distribution 7 is in better agreement with observations than distribution 2, because the spectrum has fallen significantly at 2 kHz and the dashed red curve in Fig. 8a is above 2 kHz for most of the relevant angle range of $\alpha \lesssim 50°$ determined above. The dashed black curve is close to 1 kHz in this range, and it is in good agreement with the peak of the spectrum in Fig. 3. Of the different dispersion relations we have examined it is the one corresponding to distribution 7 that best fits the Rosetta data. However, several distributions can lead to similar growth rates at similar frequencies, and we cannot constrain the distribution function closely. What we can say is that distributions that lead to moderate growth rates are in better agreement with the data than those that show very rapid growth.

Fig. 8b shows the Doppler shifted ion plasma frequency and frequency of maximum growth for distribution A. The real part of the dispersion relation for distributions A and B overlap in Fig. 7, and therefore the Doppler shifted ion plasma frequency will be the same for distribution B as for distribution A. For distribution B the waves are damped everywhere, and there is no frequency of maximum growth. We have already concluded in Sect. 3 that distribution B is more likely than distribution A, and that the waves that were observed as the spacecraft moved away were not generated at the spacecraft location. The frequency where the wave power peaks tells us more about the source region than about the conditions at the spacecraft position. The blue curve in Fig. 3 has fallen to the noise floor at approximately 3 kHz, and from the solid curve in Fig. 8b the dispersion relation is seen to be in agreement with data for angles in the range $\alpha \lesssim 70°$.

5 Discussion and conclusions

We have analysed data obtained during Rosetta's close flyby of comet 67P on 28 March 2015. Waves which we interpret as current-driven ion acoustic waves were recorded by the Langmuir probe instrument RPC-LAP. These waves were seen all the time the spacecraft was close to the nucleus and the wave power started to decrease at approximately 24 km cometocentric distance. We estimated the current density from magnetic field measurements and found that the same currents that are involved in draping and pileup of the magnetic field (Koenders et al., 2016) are sufficient to drive the ion acoustic mode unstable, according to the kinetic model we have used to compute dispersion relations. Koenders et al. (2016) could observe field line draping until the rapid magnetic field change that occurred at 20:42 when Rosetta was at 34 km cometocentric distance.

https://doi.org/10.5194/angeo-2020-59
Preprint. Discussion started: 18 August 2020
© Author(s) 2020. CC BY 4.0 License.

Data from RPC-LAP indicate the presence of two electron populations, one cold at temperature around 0.2 eV and one warm at $\sim 4\,\mathrm{eV}$. Furthermore, the RPC-LAP characteristics show the presence of a cold ion population drifting with a speed between $3\,\mathrm{km\,s^{-1}}$ and $3.7\,\mathrm{km\,s^{-1}}$. This component of the ion distribution went undetected by the ion spectrometer RPC-ICA. Instead a warm, several electron volts in temperature, ion distribution was detected by RPC-ICA, but its density is not sufficient for it to have any significant influence on the waves.

We are not able to measure the fine details of the particle distributions. However, by testing different assumptions about the distributions it is possible to say something about it. We have seen that the best agreement between the theoretical dispersion relations and the observed wave spectra is obtained when the growth rate is moderate. This can be achieved with a cold ion distribution with $k_\mathrm{B}T = 0.04\,\mathrm{eV}$. This is the warmest cold distribution that we tried, but it is still a very low temperature compared to all the other charged particle populations. The same result may be obtained with a lower temperature, if there also are suprathermal particles present. To accurately measure distribution functions at such low energies would represent a challenge in space-based instrumentation. These cold ion temperatures are reasonable, considering that Biver et al. (2019) found neutral temperatures up to approximately $0.02\,\mathrm{eV}$ between the nucleus and $15\,\mathrm{km}$ cometocentric distance. The ion distribution is formed by ionisation of the neutrals, and initially the neutral and ion temperatures are the same. On their way out to the spacecraft position, the ions may undergo some heating either through an increased the bulk temperature or by forming suprathermal tails. To summarise the result of computing dispersion relations for different distributions, it is distribution 7 in Table 1 that shows the best agreement with observations. It has the warmest cold ion distribution ($0.04\,\mathrm{eV}$), the current carried by the cold electrons, and no warm ion component as that was found to be negligible.

By computing the Doppler shift and comparing observed spectra with wave theory and known properties of current-driven ion acoustic waves we can estimate the angle between the bulk velocity of the cold ions and the propagation direction of the waves to be $\alpha \lesssim 50°$ for closest approach and $\alpha \lesssim 70°$ farther out when Rosetta was moving away and the wave power decreasing. Previous estimates have shown that ions move away from the centre of the comet, predominantly in a radial direction (Odelstad et al., 2018) as would be expected if they are accelerated by the ambipolar field present in the inner coma (Gunell et al., 2019). There are also observations of ions with an anti-sunward velocity component (Berčič et al., 2018), but those ions were faster than the (3–3.7) $\mathrm{km\,s^{-1}}$ we have observed here. If we assume that the ions move radially outward, the estimate of $\alpha \lesssim 50°$ for the waves near closest approach will also apply to the angle between the direction of propagation and the radial direction. Waves should propagate in the direction of the relative velocity between the electrons and the ions, and our angle estimates must not be seen as general results. They apply only at the position of the spacecraft during the flyby and for the orientation of the current at the time. During the outbound pass of the spacecraft, the angle of propagation cannot be restricted more than to say that it is below 70°. Here, Rosetta was likely outside the source region, and the waves propagated to the spacecraft from a source located closer to the nucleus.

We only have information about the waves along a single spacecraft trajectory, and what we know about the current comes from crude estimates based on single spacecraft magnetic field observations. To obtain a more complete picture of currents and waves in the inner coma would require the comet to be accompanied by multiple spacecraft collecting data at the same time (Götz et al., 2019).

https://doi.org/10.5194/angeo-2020-59
Preprint. Discussion started: 18 August 2020
© Author(s) 2020. CC BY 4.0 License.
Annales Geophysicae
Discussions

Code and data availability. The Rosetta data sets are available at the ESA Planetary Science Archive <https://archives.esac.esa.int/psa>. The specific data set used in this article is available at <https://doi.org/10.5281/zenodo.3973232> together with computer codes to produce the figures (Gunell et al., 2020). *Note: the doi has been reserved and the data set will be published there upon acceptance of this article.*

Appendix A: The influence of suprathermal particles

As mentioned in the main text the index m controls the thickness of the suprathermal tails of the distribution function. In distributions 1–7, $m = 3$ for the ions and $m = 5$ for the electrons. For comparison we have performed calculations with $m = 6$ and $m = 8$ for all populations. These are shown in Fig. A1 as distributions 8 and 9 by the red and blue curve respectively. In both cases the cold ion temperature was 0.02 eV, and for comparison the dispersion relation for distribution 6, which has 0.01 eV cold ions, is also shown in Fig. A1. The results are very similar, and we conclude that the influence on the dispersion relation from the suprathermal tails is similar to the difference between distributions with 0.01 and 0.02 eV ions. Since we cannot directly measure the distribution function at these low energies we cannot tell the two effects apart. The distributions with higher m indeces shown in Fig. A1 and those in Fig. 6 both agree with observations within the limits of experimental uncertainty.

Author contributions. HG performed the analysis in collaboration with CG, who also was the one to identify the flyby as an item of interest for wave studies, and EO, who in particular contributed to the plasma characterisation based on Langmuir probe data. All authors contributed to the writing of the final manuscript.

Competing interests. The authors declare that they have no competing interests.

Acknowledgements. This work was supported by the Swedish National Space Agency (grants 96/15 and 108/18). CG was supported by an ESA Research Fellowship. Work at LPC2E/CNRS was supported by CNES and by ANR under the financial agreement ANR-15-CE31-0009-01.

https://doi.org/10.5194/angeo-2020-59
Preprint. Discussion started: 18 August 2020
© Author(s) 2020. CC BY 4.0 License.

Annales Geophysicae
Discussions

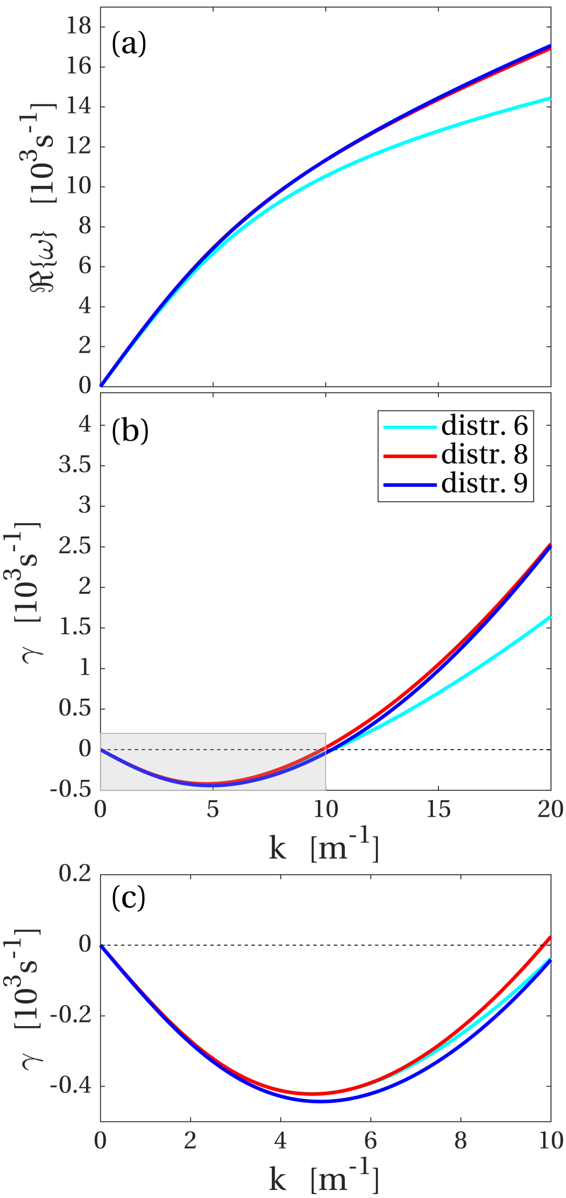

Figure A1. Dispersion relations for distributions with different suprathermal tails. Distribution 6 is the same as the distribution with that number shown in Fig. 6, and it has $m = 3$ for the ions and $m = 5$ for each of the two electron populations. Distribution 8 has $m = 6$ and distribution 9 $m = 8$ for all three populations. (a) real part of the dispersion relation. (b) damping rate γ. (c) zoom-in on the shaded rectangle in panel (b).

https://doi.org/10.5194/angeo-2020-59
Preprint. Discussion started: 18 August 2020
© Author(s) 2020. CC BY 4.0 License.

Annales Geophysicae
Discussions
Open Access
EGU

References

André, M., Odelstad, E., Graham, D. B., Eriksson, A. I., Karlsson, T., Stenberg Wieser, G., Vigren, E., Norgren, C., Johansson, F. L., Henri, P., Rubin, M., and Richter, I.: Lower hybrid waves at comet 67P/Churyumov-Gerasimenko, Monthly Notices of the Royal Astronomical Society, 469, S29–S38, https://doi.org/10.1093/mnras/stx868, 2017.

Berčič, L., Behar, E., Nilsson, H., Nicolaou, G., Stenberg Wieser, G., Wieser, M., and Goetz, C.: Cometary ion dynamics observed in the close vicinity of comet 67P/Churyumov-Gerasimenko during the intermediate activity period, Astronomy & Astrophysics, 613, A57, https://doi.org/10.1051/0004-6361/201732082, 2018.

Bergman, S., Stenberg Wieser, G., Wieser, M., Johansson, F. L., and Eriksson, A.: The Influence of Spacecraft Charging on Low-Energy Ion Measurements Made by RPC-ICA on Rosetta, J. Geophys. Res. (Space Physics), 125, e2019JA027 478, https://doi.org/10.1029/2019JA027478, 2020a.

Bergman, S., Stenberg Wieser, G., Wieser, M., Johansson, F. L., and Eriksson, A.: The Influence of Varying Spacecraft Potentials and Debye Lengths on In Situ Low-Energy Ion Measurements, J. Geophys. Res. (Space Physics), 125, e2020JA027 870, https://doi.org/10.1029/2020JA027870, 2020b.

Biver, N., Bockelée-Morvan, D., Hofstadter, M., Lellouch, E., Choukroun, M., Gulkis, S., Crovisier., J., Schloerb, F. P., Rezac, L., von Allmen, P., Lee, S., Leyrat, C., Ip, W. H., Hartogh, P., Encrenaz, P., Beaudin, G., and the MIRO Team: Long-term monitoring of the outgassing and composition of comet 67P/Churyumov-Gerasimenko with the Rosetta/MIRO instrument, Astronomy & Astrophysics, 630, A19, https://doi.org/10.1051/0004-6361/201834960, 2019.

Breuillard, H., Henri, P., Bucciantini, L., Volwerk, M., Karlsson, T., Eriksson, A., Johansson, F., Odelstad, E., Richter, I., Goetz, C., Vallières, X., and Hajra, R.: The properties of the singing comet waves in the 67P/Churyumov–Gerasimenko plasma environment as observed by the Rosetta mission, Astronomy & Astrophysics, https://doi.org/10.1051/0004-6361/201834876, 2019.

Carr, C., Cupido, E., Lee, C. G. Y., Balogh, A., Beek, T., Burch, J. L., Dunford, C. N., Eriksson, A. I., Gill, R., Glassmeier, K. H., Goldstein, R., Lagoutte, D., Lundin, R., Lundin, K., Lybekk, B., Michau, J. L., Musmann, G., Nilsson, H., Pollock, C., Richter, I., and Trotignon, J. G.: RPC: The Rosetta Plasma Consortium, Space Science Reviews, 128, 629–647, https://doi.org/10.1007/s11214-006-9136-4, 2007.

Engelhardt, I. A. D., Eriksson, A. I., Vigren, E., Valliéres, X., Rubin, M., Gilet, N., and Henri, P.: Cold electrons at comet 67P/Churyumov-Gerasimenko, Astronomy & Astrophysics, 616, A51, https://doi.org/10.1051/0004-6361/201833251, 2018.

Eriksson, A. I., Boström, R., Gill, R., Åhlén, L., Jansson, S.-E., Wahlund, J.-E., André, M., Mälkki, A., Holtet, J. A., Lybekk, B., Pedersen, A., and Blomberg, L. G.: RPC-LAP: The Rosetta Langmuir Probe Instrument, Space Science Reviews, 128, 729–744, https://doi.org/10.1007/s11214-006-9003-3, 2007.

Eriksson, A. I., Engelhardt, I. A. D., André, M., Boström, R., Edberg, N. J. T., Johansson, F. L., Odelstad, E., Vigren, E., Wahlund, J.-E., Henri, P., Lebreton, J.-P., Miloch, W. J., Paulsson, J. J. P., Wedlund, C. S., Yang, L., Karlsson, T., Broiles, T., Mandt, K., Carr, C. M., Galand, M., Nilsson, H., and Norberg, C.: Cold and warm electrons at comet 67P/Churyumov-Gerasimenko, Astronomy & Astrophysics, 605, A15, https://doi.org/10.1051/0004-6361/201630159, 2017.

Glassmeier, K.-H., Boehnhardt, H., Koschny, D., Kührt, E., and Richter, I.: The Rosetta Mission: Flying Towards the Origin of the Solar System, Space Science Reviews, 128, 1–21, https://doi.org/10.1007/s11214-006-9140-8, 2007a.

Glassmeier, K.-H., Richter, I., Diedrich, A., Musmann, G., Auster, U., Motschmann, U., Balogh, A., Carr, C., Cupido, E., Coates, A., Rother, M., Schwingenschuh, K., Szegö, K., and Tsurutani, B.: RPC-MAG The Fluxgate Magnetometer in the ROSETTA Plasma Consortium, Space Science Reviews, 128, 649–670, https://doi.org/10.1007/s11214-006-9114-x, 2007b.

https://doi.org/10.5194/angeo-2020-59
Preprint. Discussion started: 18 August 2020
© Author(s) 2020. CC BY 4.0 License.

Goetz, C., Koenders, C., Hansen, K. C., Burch, J., Carr, C., Eriksson, A., Frühauff, D., Güttler, C., Henri, P., Nilsson, H., Richter, I., Rubin, M., Sierks, H., Tsurutani, B., Volwerk, M., and Glassmeier, K. H.: Structure and evolution of the diamagnetic cavity at comet 67P/Churyumov-Gerasimenko, Monthly Notices of the Royal Astronomical Society, 462, S459, https://doi.org/10.1093/mnras/stw3148, 2016a.

Goetz, C., Koenders, C., Richter, I., Altwegg, K., Burch, J., Carr, C., Cupido, E., Eriksson, A., Güttler, C., Henri, P., Mokashi, P., Nemeth, Z., Nilsson, H., Rubin, M., Sierks, H., Tsurutani, B., Vallat, C., Volwerk, M., and Glassmeier, K.-H.: First detection of a diamagnetic cavity at comet 67P/Churyumov-Gerasimenko, Astronomy & Astrophysics, 588, A24, https://doi.org/10.1051/0004-6361/201527728, 2016b.

Goetz, C., Plaschke, F., and Taylor, M. G. G. T.: Singing Comet Waves in a Solar Wind Convective Electric Field Frame, Geophysical Research Letters, 47, e2020GL087 418, https://doi.org/10.1029/2020GL087418, 2020.

Götz, C., Gunell, H., Volwerk, M., Beth, A., Eriksson, A., Galand, M., Henri, P., Nilsson, H., Wedlund, C. S., Alho, M., Andersson, L., Andre, N., De Keyser, J., Deca, J., Ge, Y., Glaßmeier, K.-H., Hajra, R., Karlsson, T., Kasahara, S., Kolmasova, I., LLera, K., Madanian, H., Mann, I., Mazelle, C., Odelstad, E., Plaschke, F., Rubin, M., Sanchez-Cano, B., Snodgrass, C., and Vigren, E.: Cometary Plasma Science – A White Paper in response to the Voyage 2050 Call by the European Space Agency, arXiv e-prints, arXiv:1908.00377, https://arxiv.org/pdf/1908.00377.pdf, 2019.

Gunell, H. and Skiff, F.: Weakly damped acoustic-like ion waves in plasmas with non-Maxwellian ion distributions, Physics of Plasmas, 8, 3550–3557, https://doi.org/10.1063/1.1386428, 2001.

Gunell, H. and Skiff, F.: Electrostatic fluctuations in plasmas with distribution functions described by simple pole expansions, Physics of Plasmas, 9, 2585–2592, https://doi.org/10.1063/1.1476666, 2002.

Gunell, H., Goetz, C., Eriksson, A., Nilsson, H., Simon Wedlund, C., Henri, P., Maggiolo, R., Hamrin, M., De Keyser, J., Rubin, M., Stenberg Wieser, G., Cessateur, G., Dhooghe, F., and Gibbons, A.: Plasma waves confined to the diamagnetic cavity of comet 67P/Churyumov-Gerasimenko, Monthly Notices of the Royal Astronomical Society, 469, S84, https://doi.org/10.1093/mnras/stx1134, 2017a.

Gunell, H., Nilsson, H., Hamrin, M., Eriksson, A., Odelstad, E., Maggiolo, R., Henri, P., Vallières, X., Altwegg, K., Tzou, C.-Y., Rubin, M., Glassmeier, K.-H., Stenberg Wieser, G., Simon Wedlund, C., De Keyser, J., Dhooghe, F., Cessateur, G., and Gibbons, A.: Ion acoustic waves at comet 67P/Churyumov-Gerasimenko – Observations and computations, Astronomy & Astrophysics, 600, A3, https://doi.org/10.1051/0004-6361/201629801, 2017b.

Gunell, H., Goetz, C., Simon Wedlund, C., Lindkvist, J., Hamrin, M., Nilsson, H., LLera, K., Eriksson, A., and Holmström, M.: The infant bow shock: a new frontier at a weak activity comet, Astronomy & Astrophysics, 619, L2, https://doi.org/10.1051/0004-6361/201834225, 2018.

Gunell, H., Lindkvist, J., Goetz, C., Nilsson, H., and Hamrin, M.: Polarisation of a small-scale cometary plasma environment: Particle-in-cell modelling of comet 67P/Churyumov-Gerasimenko, Astronomy & Astrophysics, 631, A174, https://doi.org/10.1051/0004-6361/201936004, 2019.

Gunell, H., Goetz, C., Odelstad, E., Beth, A., Hamrin, M., Henri, P., Johansson, F. L., Nilsson, H., and Wieser, G. S.: Dataset for Waves during Rosetta's close flyby of comet 67P, https://doi.org/10.5281/zenodo.3973232, 2020.

Karlsson, T., Eriksson, A. I., Odelstad, E., André, M., Dickeli, G., Kullen, A., Lindqvist, P.-A., Nilsson, H., and Richter, I.: Rosetta measurements of lower hybrid frequency range electric field oscillations in the plasma environment of comet 67P, Geophys. Res. Lett., 44, 1641–1651, https://doi.org/10.1002/2016GL072419, 2017.

Kawai, Y., Hollenstein, C., and Guyot, M.: Ion acoustic turbulence in a large-volume plasma, Physics of Fluids, 21, 970–974, https://doi.org/10.1063/1.862340, 1978.

Koenders, C., Goetz, C., Richter, I., Motschmann, U., and Glassmeier, K.-H.: Magnetic field pile-up and draping at intermediately active comets: results from comet 67P/Churyumov-Gerasimenko at 2.0 AU, Monthly Notices of the Royal Astronomical Society, 462, S235–S241, https://doi.org/10.1093/mnras/stw2480, 2016.

Krall, N. A. and Trivelpiece, A. W.: Principles of Plasma Physics, McGraw-Hill, New York, 1973.

Löfgren, T. and Gunell, H.: Flexible Simple-Pole Expansion of Distribution Functions, Physics of Plasmas, 4, 3469–3476, https://doi.org/10.1063/1.872243, 1997.

Madsen, B., Simon Wedlund, C., Eriksson, A., Goetz, C., Karlsson, T., Gunell, H., Spicher, A., Henri, P., Vallières, X., and Miloch, W.: Extremely low-frequency waves inside the diamagnetic cavity of comet 67P/Churyumov-Gerasimenko, Geophys. Res. Lett., 45, 3854–3864, https://doi.org/10.1029/2017GL076415, 2018.

Meier, P., Glassmeier, K.-H., and Motschmann, U.: Modified ion-Weibel instability as a possible source of wave activity at Comet 67P/Churyumov-Gerasimenko, Annales Geophysicae, 34, 691–707, https://doi.org/10.5194/angeo-34-691-2016, 2016.

Mott-Smith, H. M. and Langmuir, I.: The Theory of Collectors in Gaseous Discharges, Physical Review, 28, 727–763, https://doi.org/10.1103/PhysRev.28.727, 1926.

Nilsson, H., Lundin, R., Lundin, K., Barabash, S., Borg, H., Norberg, O., Fedorov, A., Sauvaud, J.-A., Koskinen, H., Kallio, E., Riihelä, P., and Burch, J. L.: RPC-ICA: The Ion Composition Analyzer of the Rosetta Plasma Consortium, Space Science Reviews, 128, 671–695, https://doi.org/10.1007/s11214-006-9031-z, 2007.

Odelstad, E., Eriksson, A. I., Johansson, F. L., Vigren, E., Henri, P., Gilet, N., Heritier, K. L., Vallières, X., Rubin, M., and André, M.: Ion Velocity and Electron Temperature Inside and Around the Diamagnetic Cavity of Comet 67P, J. Geophys. Res. (Space Physics), 123, 5870–5893, https://doi.org/10.1029/2018JA025542, 2018.

Oya, H., Morioka, A., Miyake, W., Smith, E. J., and Tsurutani, B. T.: Discovery of cometary kilometric radiations and plasma waves at comet Halley, Nature, 321, 307–310, https://doi.org/10.1038/321307a0, 1986.

Richter, I., Koenders, C., Auster, H.-U., Frühauff, D., Götz, C., Heinisch, P., Perschke, C., Motschmann, U., Stoll, B., Altwegg, K., Burch, J., Carr, C., Cupido, E., Eriksson, A., Henri, P., Goldstein, R., Lebreton, J.-P., Mokashi, P., Nemeth, Z., Nilsson, H., Rubin, M., Szegö, K., Tsurutani, B. T., Vallat, C., Volwerk, M., and Glassmeier, K.-H.: Observation of a new type of low-frequency waves at comet 67P/Churyumov-Gerasimenko, Annales Geophysicae, pp. 1031–1036, https://doi.org/10.5194/angeo-33-1031-2015, 2015.

Richter, I., Auster, H.-U., Berghofer, G., Carr, C., Cupido, E., Fornaçon, K.-H., Goetz, C., Heinisch, P., Koenders, C., Stoll, B., Tsurutani, B. T., Vallat, C., Volwerk, M., and Glassmeier, K.-H.: Two-point observations of low-frequency waves at 67P/Churyumov-Gerasimenko during the descent of PHILAE: comparison of RPCMAG and ROMAP, Annales Geophysicae, 34, 609–622, https://doi.org/10.5194/angeo-34-609-2016, 2016.

Scarf, F.: Plasma wave observations at Comets Giacobini-Zinner and Halley, Washington DC American Geophysical Union Geophysical Monograph Series, 53, 31–40, https://doi.org/10.1029/GM053p0031, 1989.

Scarf, F. L., Coroniti, F. V., Kennel, C. F., Sanderson, T. R., Wenzel, K. P., Hynds, R. J., Smith, E. J., Bame, S. J., and Zwickl, R. D.: ICE plasma wave measurements in the ion pick-up region of comet Halley, Geophys. Res. Lett., 13, 857–860, https://doi.org/10.1029/GL013i008p00857, 1986a.

Scarf, F. L., Ferdinand, V., Coroniti, V., Kennel, C. F., Gurnett, D. A., Ip, W.-H., and Smith, E. J.: Plasma wave observations at comet Giacobini-Zinner, Science, 232, 377–381, https://doi.org/10.1126/science.232.4748.377, 1986b.

Scarf, F. L., Ferdinand, V., Coroniti, V., Kennel, C. F., Gurnett, D. A., Ip, W.-H., and Smith, E. J.: Plasma wave observations at comet Giacobini-Zinner, Science, 232, 377–381, https://doi.org/10.1126/science.232.4748.377, 1986c.

https://doi.org/10.5194/angeo-2020-59
Preprint. Discussion started: 18 August 2020
© Author(s) 2020. CC BY 4.0 License.

Annales Geophysicae Discussions

Stenberg Wieser, G., Odelstad, E., Nilsson, H., Wieser, M., Goetz, C., Karlsson, T., Kalla, L., André, M., Eriksson, A. I., Nicolaou, G., Simon Wedlund, C., Richter, I., and Gunell, H.: Investigating short time-scale variations in cometary ions around comet 67P, Monthly Notices of the Royal Astronomical Society, 469, S522–S534, https://doi.org/10.1093/mnras/stx2133, 2017.

Swift, J. D. and Schwar, M. J. R.: Electrical Probes for Plasma Diagnostics, Iliffe Books, London, 1970.

Tjulin, A. and André, M.: The dielectric tensor of simple-pole distribution functions in magnetized plasmas, Physics of Plasmas, 9, 1775–1784, https://doi.org/10.1063/1.1463410, 2002.

Tjulin, A., Eriksson, A. I., and André, M.: Physical interpretation of the Padé approximation of the plasma dispersion function, Journal of Plasma Physics, 64, 287–296, https://doi.org/10.1017/S0022377800008606, 2000.

Trotignon, J. G., Michau, J. L., Lagoutte, D., Chabassière, M., Chalumeau, G., Colin, F., Décréau, P. M. E., Geiswiller, J., Gille, P., Grard, R., Hachemi, T., Hamelin, M., Eriksson, A., Laakso, H., Lebreton, J. P., Mazelle, C., Randriamboarison, O., Schmidt, W., Smit, A., Telljohann, U., and Zamora, P.: RPC-MIP: the Mutual Impedance Probe of the Rosetta Plasma Consortium, Space Science Reviews, 128, 713–728, https://doi.org/10.1007/s11214-006-9005-1, 2007.

Wattieaux, G., Henri, P., Gilet, N., Vallières, X., and Deca, J.: Plasma characterization at comet 67P between 2 and 4 AU from the Sun with the RPC-MIP instrument, Astronomy & Astrophysics, 638, A124, https://doi.org/10.1051/0004-6361/202037571, 2020.

Welch, P. D.: The Use of Fast Fourier Transform for the Estimation of Power Spectra: A Method Based on Time Averaging Over Short, Modified Periodograms, IEEE Trans. Audio and Electroacoust, AU–15, 70–73, 1967.